The Astrophysical Journal, 1004:203 (9pp), 2026 June 20 https://doi.org/10.3847/1538-4357/ae6dab

Coronal Mass Ejection and Heliospheric Current Sheet Interaction Causing a Long-duration Magnetic Field Sector Transition

Manuela Temmer[1], Stephan G. Heinemann[1,2], Nina Dresing[3], Mateja Dumbovic[4], and Eleanna Asvestari[2]
[1] Institute of Physics, University of Graz, Austria; manuela.temmer@uni-graz.at
[2] Department of Physics, University of Helsinki, Finland
[3] Department of Physics and Astronomy, University of Turku, Finland
[4] Hvar Observatory, Faculty of Geodesy, University of Zagreb, Croatia
Received 2025 December 11; revised 2026 May 11; accepted 2026 May 12; published 2026 June 15

Abstract

We present a study that combines remote-sensing and in situ observations of coronal mass ejections (CMEs) interacting with the nearby heliospheric current sheet (HCS). The sequence of eruptive events under study culminates in the largest directly observed flare of solar cycle 25 on 2024 October 3, producing a fast halo CME. Their source region can be linked to a so-called nested active region (or active longitude) that persisted over several solar rotations. Such long-lived regions reflect deep-seated magnetic structures that shape the global magnetic field configuration. By applying the drag-based CME propagation model, we connect the near-Sun observations from several CMEs during that activity period with in situ measurements. While one of the CMEs propagated on the opposite side of the HCS from Earth, and therefore did not produce in situ signatures near Earth, we detect, over the period 2024 October 5–10, a complex of HCS and CME structures propagating together with a shock ahead of them. The HCS seems to be locally replaced by the CME signatures, leading to a long-duration sector reversal of more than 48 hr. This event highlights the intrinsic connection between solar surface structures, the global magnetic field, and the evolution of complex eruptive events.

Unified Astronomy Thesaurus concepts: Solar wind (1534); Solar coronal mass ejections (310); Solar activity (1475)

1. Introduction

Major energy release in flares—and therefore the occurrence of X-class flares in active regions (ARs)—is typically linked to the complexity of their magnetic fields (I. Sammis et al. 2000). Studies have shown that clusters of complex ARs are not uniformly distributed across the Sun but tend to form at preferred longitudes (the so-called active longitudes, active zones, or nested ARs; e.g., G. de Toma et al. 2000; S. V. Berdyugina & I. G. Usoskin 2003; A. Q. Chen et al. 2011). These nests can persist for months to years due to the repeated emergence of magnetic flux and therefore may exert a significant influence on the structure of the solar global magnetic field (V. Gaizauskas et al. 1983; L. van Driel-Gesztelyi & L. M. Green 2015). Recent work reports that the heliospheric current sheet (HCS) can become anchored above nested ARs and, owing to the continual flux emergence, become substantially warped (A. J. Finley 2024). Spatial overlaps have also been found between hard X-ray flare locations and Hale sector boundaries (K. Loumou et al. 2018), which are segments of the HCS (L. Svalgaard & J. M. Wilcox 1976). More recent results further confirm that AR nests host the most energetic flares (e.g., for solar cycle 24; A. J. Finley et al. 2025), including those responsible for the strongest geomagnetic storms of solar cycle 25 in 2024 May (I. Kontogiannis et al. 2025).

The large-scale magnetic topology in the solar corona is shaped by the distribution of open and closed magnetic field structures, such as ARs and coronal holes. Coronal mass ejections (CMEs) drive significant changes in this topology. Fast CMEs typically comprise a shock and sheath driven by magnetic ejecta, which often manifest as flux ropes (FRs; see, e.g., T. H. Zurbuchen & I. G. Richardson 2006). These magnetic structures tend to align with the global magnetic configuration, particularly the orientation of the HCS (e.g., V. B. Yurchyshyn et al. 2001), or get deflected away from open flux regions such as coronal holes, which are spatially closely related to the HCS structure (H. Cremades et al. 2006; N. Gopalswamy et al. 2009; S. G. Heinemann et al. 2019). The coronal topology and its continuation farther out in interplanetary space can get strongly distorted by transient events, namely CMEs (e.g., M. J. Owens & R. J. Forsyth 2013). CMEs therefore may have important effects on the HCS itself in terms of shape and local orientation (e.g., J. J. Blanco et al. 2011; E. K. J. Kilpua et al. 2022; O. M. Romeo et al. 2023).

In this study, we focus on the magnetic field sector change occurring in in situ measurements between 2024 October 5 and 9. Several CMEs released from the Sun between 2024 October 1 and 4 most likely have interacted with the heliospheric plasma sheet (HPS) surrounding the HCS, leading to a long-duration sector change. We investigate the CME source regions in relation to the HCS to provide a detailed explanation of the structures observed during this period of magnetic sector polarity reversal. We aim to give a consistent picture relating the strongest (as of 2026 May) directly observed flare from solar cycle 25 (X9.0 from 2024 October 3; see more details on the flare in T. Ding et al. 2025) to the CME and its in situ measured signals at 1 au. While to some extent it is statistically established that the correlation between CME-related flare intensity and geomagnetic impact is weak (e.g., T. A. Howard & S. J. Tappin 2005; J. Zhang et al. 2007), with our analysis we offer an explanation as to why large flares may not produce most strongly geoeffective events.

2. Data, Methods, and Results

On 2024 October 3 at 12:18 UT, the peak of an energetic X9.0 flare from AR3842 was recorded. It was associated with an eruption that produced a halo CME with the source region location in Stonyhurst heliographic coordinates W03/S20. This event represents the strongest energy release from AR3842, with several CMEs erupting from that region in the days before (including an X7.1 flare) and after, spanning 2024 October 1–4.

The Community Coordinated Modeling Center (CCMC) at NASA provides the publicly available Space Weather Database Of Notifications, Knowledge, Information (DONKI).[5] DONKI is meticulously populated and maintained by the Moon to Mars (M2M) Space Weather Analysis office at the Goddard Space Flight Center. There, CME 3D parameters (direction, speed, and size) are derived using the Space Weather Prediction Center CME Analysis Tool tool (SWPC-CAT; G. Millward et al. 2013) developed by NOAA and maintained at CCMC. These parameters are typically used as input for CME propagation models. Inspecting additional EUV data from the Atmospheric Imaging Assembly (AIA; J. R. Lemen et al. 2012) instrument on board the Solar Dynamics Observatory (SDO; W. D. Pesnell et al. 2012) together with the DONKI list, we find six CMEs that occurred during 2024 October 1–4.[6] Table 1 summarizes the source region, flare association, and appearance time in the LASCO/C2 coronagraph (G. E. Brueckner et al. 1995) on board the Solar and Heliospheric Observatory (SOHO; V. Domingo et al. 1995). It also includes 3D characteristics of the CMEs, where for certain events, the shock and leading-edge information are provided separately.

To investigate geoeffective and potentially interacting CMEs, we focus first on the three fastest events listed in Table 1: CME1, CME4, and CME5, all of which have shock speeds exceeding 850 km s^{-1}. Figure 1 shows the solar corona in SDO/AIA EUV three-channel running-ratio images and LASCO/C2 data. CME1 is associated with an X7.1 flare and CME4 is associated with an X9.0 flare. Both are launched from AR3842 and produced coronal waves and large-scale dimming regions, indicative of strongly expanding CMEs. CME5 is associated with an M6.7 flare from AR3843. All CMEs exhibit halo signatures in white-light data. CME1 and CME4, whose source regions are associated with AR3842 near the central meridian, have the highest potential to be detected in situ at Earth.

Figure 2 shows synchronous maps (see F. Auchère et al. 2005) from SDO/AIA 304 Å images of the southern hemisphere, covering the time range 2024 April–October. The boxes indicate so-called nested ARs, which are of particular interest. Over that period, we identify two active bands on the Sun that persist over several rotations. One band (yellow dashed line) covers AR3842, which is the main source region of the 2024 October 1–4 events under study (see Table 1). The other band (gray dashed line), separated in longitude by about 180° (see also I. G. Usoskin et al. 2005), is related to the AR producing the so-called 2024 May events, which caused the highly geoeffective Mother's Day or Gannon storm (see, e.g., the flash report by H. Hayakawa et al. 2025). A recent study by I. Kontogiannis et al. (2025), which examined the magnetic-field evolution of the source region of the 2024 May geomagnetic storms from a 360° perspective, confirms that it was associated with a nested AR that was supplied by emerging magnetic flux over several months. With that we want to highlight that the source region of the strongest flare observed on the Sun's nearside of solar cycle 25 (as of 2026 May) is also linked to a nested AR that persisted for at least 6 months.

To infer the relation between that nested AR and the global magnetic field configuration, we derive the HCS location. To account for uncertainties, we use different magnetic data sources, namely the synoptic Heliospheric and Magnetic Imager (HMI; J. Schou et al. 2012) and the Global Oscillation Network Group (GONG; J. W. Harvey et al. 1996), as well as GONG Air Force Data Assimilative Photospheric Flux Transport (ADAPT) and HMI ADAPT (C. N. Arge et al. 2010) magnetic maps. From these data the potential field source surface was extrapolated using the model `CIDER`[7] with a source surface height of 2.5 $R_{\odot}$. This model uses a staggered finite-difference scheme to solve Laplace's equation for the scalar potential, yielding a numerically divergence- and curl-free magnetic field (similar to S. G. Heinemann et al. 2025). Figure 3 presents the HCS locations as derived from different magnetic maps for 2024 October 3, which show a consistent picture except in the polar regions, where deviations likely result from line-of-sight effects in the magnetic field measurements. We find that AR3842 is closely associated with the HCS. In this context, we investigate how this relationship influences CME evolution and their in situ characteristics, particularly those originating from AR3842.

For the in situ analysis we take measurements from OMNI in Geocentric Solar Ecliptic (GSE) coordinates, as 1 minute data time-shifted to the nose of the Earth's bow shock (J. H. King & N. E. Papitashvili 2005).[8] The OMNI dataset includes, among others, plasma and magnetic field measurements, from which we calculate the magnetic field angles in the azimuthal (ϕ_B) and polar (θ_B) direction, alpha-to-proton density ratios, and magnetic indices, such as the SYM-H index. Figure 4 presents ϕ_B, the total and vector magnetic field, proton bulk speed, and SYM-H over the time range 2024 October 3–10. Applying the drag-based CME propagation model (DBM; B. Vršnak et al. 2013; M. Dumbović et al. 2021), we infer the arrival times of the structures related to the CMEs. Columns (5)–(9) in Table 1 give the CME 3D kinematics and geometries (time at 21.5 R_s, speed at 21.5 R_s, longitude, latitude, and half-width) as taken from the CCMC/M2M catalog. Specific DBM inputs are given in columns 10 and 11 in Table 1, covering the average solar wind speed prior to CME arrival—consistent with in situ measurements—and the drag parameter, γ, which is chosen to be $0.2\cdot10^{-7}$ km^{-1} for CMEs with speeds between 600 and 1000 km s^{-1} and $0.5\cdot10^{-7}$ km^{-1} for CMEs with speeds lower than 600 km s^{-1} (see B. Vršnak et al. 2014; J. Čalogović et al. 2021). We note that an informed estimate to be put in DBM is sufficient for our purpose, as we aim to show how things relate between the Sun and in situ measurements, and not to produce an exact prediction for each CME. Columns 12 and 13 in Table 1 give

[5] https://kauai.ccmc.gsfc.nasa.gov/DONKI/

[6] https://kauai.ccmc.gsfc.nasa.gov/DONKI/search/results?startDate=2024-10-01&endDate=2024-10-04&catalog=M2M_CATALOG&eventType=ALL

[7] https://github.com/jpomoell/cider

[8] Data product: OMNI_HRO2_1MIN under https://cdaweb.gsfc.nasa.gov.

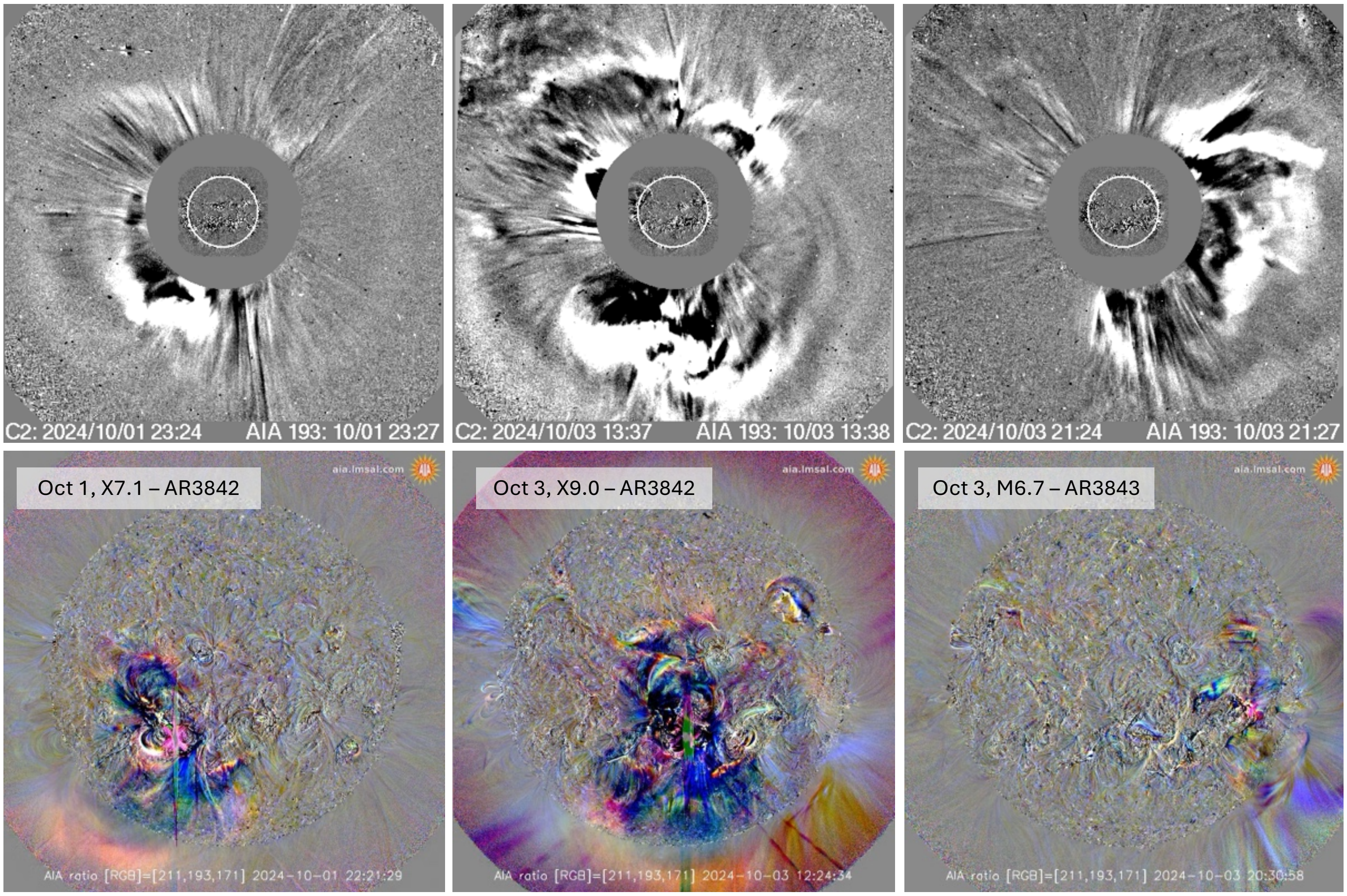

Figure 1. Solar surface and white-light structures from the three fastest and most likely Earth-directed CMEs during the activity period 2024 October 1–4. Top: LASCO/C2 white-light and inserted SDO/AIA 193 Å EUV running difference images. Bottom: SDO/AIA running-ratio EUV images from combined channels of 211, 193, and 171 Å filters.

Table 1
M2M Catalog CME Events from 2024 October 1–4, with Shock and Bright Leading Edge Treated as Separately Propagating Structures, Denoted by Indices ^{a} for the Shock and ^{b} for the Leading Edge

No.	AR	Flare	$t_{\rm LASCO}$ (UT)	CME 3D parameters at 21.5 R_s: t (UT)	v (km s^{-1})	lon (deg)	lat (deg)	ha (deg)	+DBM: $v_{\rm SW}$ (km s^{-1})	γ ($\cdot 10^{-7}$km^{-1})	Prediction at 1 au: t (UT)	v (km s^{-1})
CME 1^a	3842	X7.1	Oct 1, 23:09	Oct 2, 02:30	960	−10	−12	60	350	0.2	Oct 4, 12:00	520
CME 1^b		⋯		Oct 2, 04:20	600	−19	−10	40	350	0.2	Oct 5, 10:35	440
CME 2^b	3842	M3.6	Oct 2, 06:36	Oct 2, 15:50	360	−15	−24	25	350	0.5	⋯	⋯
CME 3^b	3842	M3.2	Oct 2, 14:24	Oct 2, 21:20	450	−7	−22	20	350	0.5	⋯	⋯
CME 4^a	3842	X9.0	Oct 3, 12:48	Oct 3, 16:30	860	−3	−4	50	350	0.2	Oct 6, 04:25	510
CME 4^b		⋯		Oct 3, 16:45	820	3	−20	40	350	0.2	⋯	⋯
CME 2^b+3^b+4^b interaction ca. at $t_{105\ R_s}$				Oct 4, 15:30[a]	500[a]	0	⋯	50	350	0.5	Oct 6, 14:00	420
CME 5^a	3843	M6.7	Oct 3, 20:36	Oct 3, 23:45	1080	41	1	50	400	0.2	Oct 6, 08:55	560
CME 5^b		⋯		Oct 4, 02:00	650	51	1	50	400	0.2	Oct 7, 11:15	460
CME 6^b	3842	M4.0	Oct 4, 05:12	Oct 4, 11:15	560	15	−59	30	400	0.5	Oct 7, 17:00	450

Notes. Further information covers the CME source region (NOAA active region (AR) number), related flare GOES SXR class, first appearance in LASCO/C2 ($t_{\rm LASCO}$), and CME 3D parameters from the M2M catalog using SWPC-CAT covering time (t) and speed (v) at a distance of 21.5 R_s, Stonyhurst heliographic longitude (lon) and latitude (lat), and half-width (ha). In addition, we extracted from OMNI in situ data the ambient solar wind speed before CME arrival ($v_{\rm SW}$) and give the drag parameter γ, used as DBM input to calculate the predicted CME arrival time and speed at 1 au. Italic values indicate arrival times, which are the least reliable as these CMEs are found to be likely to hit the spacecraft with their flanks only.
[a] Value for the interaction distance of 105 R_s.

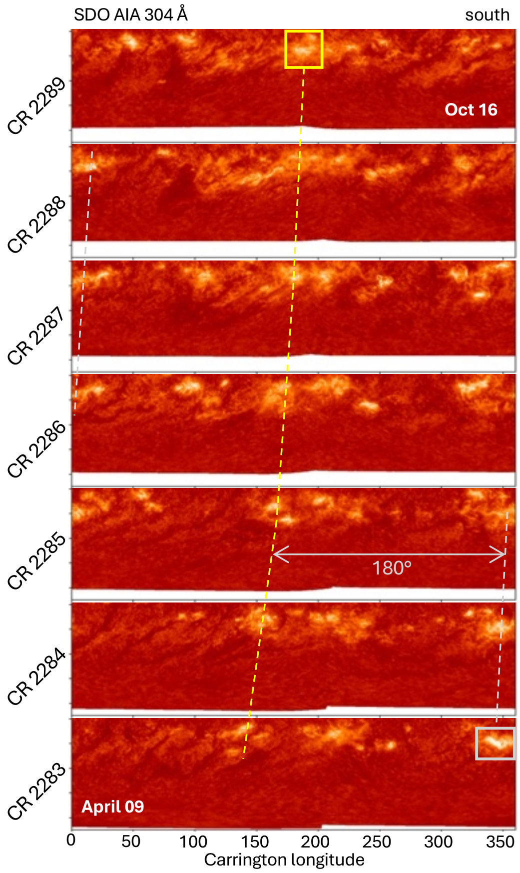

Figure 2. Synchronous maps in the 304 Å wavelength range for the period covering CR 2283–2289 (2024 April 9–October 16) using data from the AIA telescope on board SDO. The yellow box marks AR3842, related to the event under study, persisting for several solar rotations (yellow dashed line); hence, it can be related to an active longitude or nested active region. The gray box and gray dashed lines refer to the location and further evolution of the nested active region AR3664, being the source of the 2024 May storms. AR3664 and AR3842 are separated in longitude by about 180°.

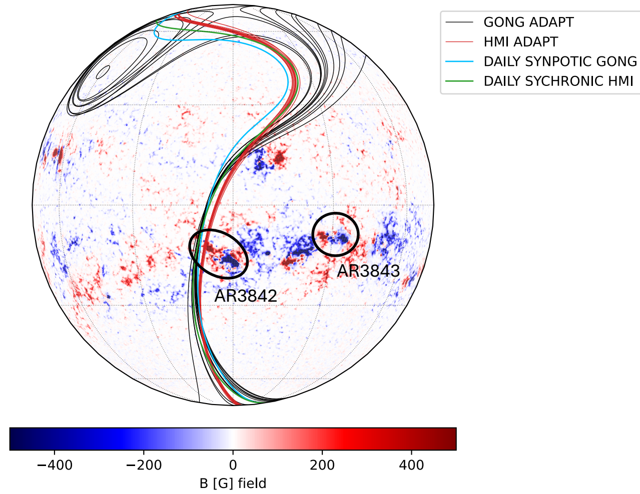

Figure 3. PFSS extrapolation using different magnetic field maps (see legend) taken on 2024 October 3, showing the HCS at a source surface height of 2.5 $R_\odot$. The active region of interest, AR3842, is lying close to the neutral line of the global magnetic field.

the DBM results covering arrival time and speed. CME1 is expected to be an isolated event, while CME2 and CME3 are interacting at a distance of about 45 R_s, and then farther with CME4 around 105 R_s. To simulate CME–CME interactions and their subsequent propagation, we adopt the approach described in J. Guo et al. (2018), in which the DBM is reinitialized at the CMEs' interaction point using its time and distance as well as average speed with changing γ accordingly. We therefore anticipate the arrival of three closely spaced FRs, associated with CME2, CME3, and CME4. This result is consistent with expectations, as all three CMEs originate from the same source region, with each successive eruption exhibiting a higher speed than its predecessor. CME5 and CME6 exhibit longitudes and latitudes indicative of glancing encounters.

We show the derived CME arrival times in Figure 4 with vertical dashed lines, labeled according to Table 1. We separately mark the shock and bright leading edge, i.e., related to the magnetic ejecta, because shocks are known to move through the magnetic structure of a CME while FRs cannot and form complex regions upon interaction (e.g., Y. Liu et al. 2012; N. Lugaz et al. 2015). Notably, we find that neither the shock nor the leading edge of CME1 caused an in situ signature within ±24 hr of the predicted arrival times on 2024 October 4–5, and therefore likely did not reach Earth. The nondetection of CME1 may be explained by the same-side/opposite-side effect (e.g., H. M. Henning et al. 1985; X. Zhao et al. 2007; M. Dumbović et al. 2021; M. Temmer et al. 2025). This condition is particularly relevant when the HCS is highly inclined, as Earth may cross into a different sector during the CME's propagation time.

A first shock signature is observed on 2024 October 6. We deduce the shock arrival time at Earth from the appearance of the associated geomagnetic sudden storm commencement, which is given at 07:39 UT. We favor this over the OMNI arrival time (07:50 UT) because OMNI time shifting is known to be less reliable for shocks, often resulting in delayed arrival times due to the use of convection-based propagation (see J. H. King & N. E. Papitashvili 2005 and the OMNI technical documentation). The maximum sheath speed is reached with ≈520 km s^{-1}. The earliest predicted arrival from the DBM corresponds to the shock of CME4 (4^a) on 2024 October 6, at 04:25 UT, with a speed of 510 km s^{-1}. This is consistent with observations assuming that the shock is not significantly affected by propagation through preceding CME magnetic structures. Under the same assumption, a likely signature of a shock from CME5 (5^a) is predicted to arrive on October 6 at 08:55 UT with a speed of 560 km s^{-1}. The interacting magnetic structures from CMEs 2+3+4 (2^b+3^b+4^b) are estimated to arrive on October 6 at 13:50 UT. The FRs associated with CME5 (5^b) and CME6 (6^b) are expected to produce, if any, only weak signatures, as both are likely glancing encounters based on their propagation directions and geometries, with predicted arrival times between October 7 11:15 and 13:00 UT. The delayed in situ signatures of the CMEs, observed up to 2024 October 8, suggest additional deceleration to CME2+3+4, likely caused by interactions with other solar wind structures. The change in the azimuthal angle from >180° before the arrival of the disturbance to <180° afterward indicates that the CMEs are associated with a magnetic sector boundary crossing lasting over 48 hr. In the following, we examine in more detail the relationship between the CMEs with this extended HCS structure.

Figure 5 covers OMNI data over the time range 2024 October 5–10. In addition, we show electron pitch-angle

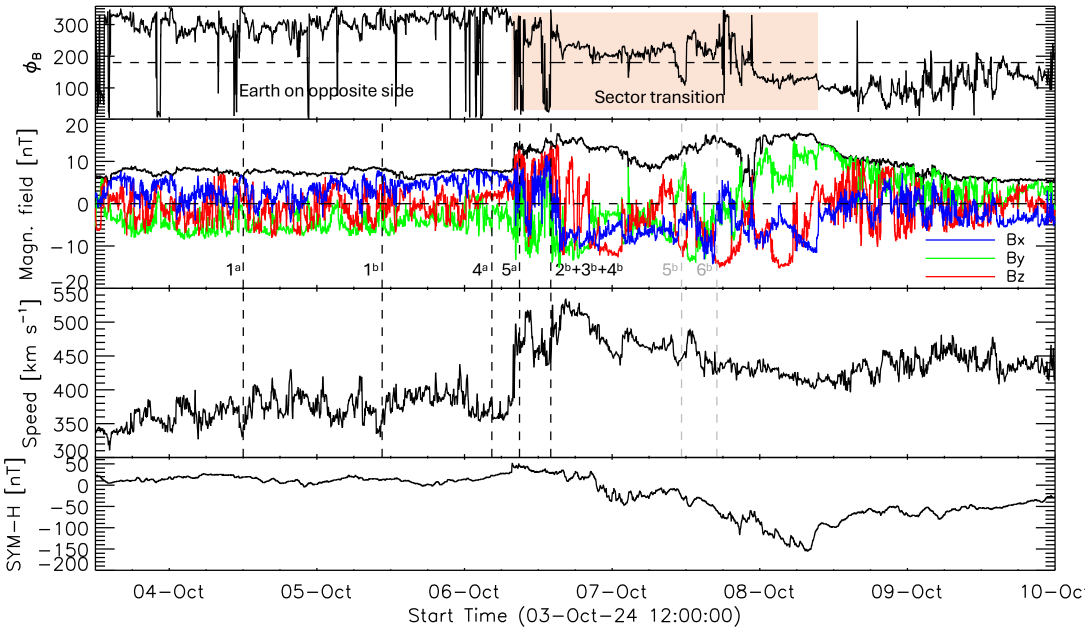

Figure 4. OMNI in situ measurements in GSE coordinates. Top to bottom: azimuthal magnetic field angle (ϕ_B), total and vector magnetic field, proton bulk speed, and SYM-H index. Vertical dashed lines show DBM results for the predicted arrival times of the CMEs as given in Table 1. Predictions for shock (^{a}) and leading edge (^{b}) are given separately. We note that 5^b and 6^b are likely glancing blows, for which we marked them in gray. The azimuthal angle shows the change in the magnetic sectors, where we marked the opposite location of AR3842 and Earth separated by the HCS.

distributions (PADs) at 175 eV from the 3DP instrument (R. P. Lin et al. 1995) and 1 minute resolution alpha-to-proton density ratios (He/p) from the L1 spacecraft Wind (K. W. Ogilvie & M. D. Desch 1997; L. B. Wilson et al. 2021). Low He/p values are found from distinct plasma around the sector-reversal region and, according to the statistical values derived by F. Xu & J. E. Borovsky (2015), He/p has a factor of 2 difference between the average value for ejecta (0.051) and sector-reversal plasma (0.024), which we use to distinguish between them. In addition, the proton temperature panel shows the expected temperature ($T_{\rm exp}$) derived from solar wind statistics, where abnormally low solar wind proton temperatures ($<0.5 \times T_{\rm exp}$) support the identification of FR structures (I. G. Richardson & H. V. Cane 1995).

We find that the azimuthal angle of the magnetic field is directed approximately along the sunward Parker spiral before the arrival of the shock. Following the shock sheath, there is a change to $\phi_B \sim 200°$, but not a full sector boundary crossing to the outward Parker spiral. As also suggested by the still enhanced temperature of the plasma, the shock-sheath region was not immediately followed by a magnetic FR structure. In fact, the low He/p values refer to a sector-reversal region (blue-shaded area in Figure 5 starting October 6, ∼14 UT), and thus to the associated HCS and HPS structures. The PAD is isotropic after the shock-sheath part, i.e., over the presumably related HPS structure. It is then followed by a period of a bidirectional electron distribution with a smooth magnetic field and low temperature, as well as enhanced He/p values, all hinting toward a FR (FR_1; October 6, 17:50 UT–October 7, 01:40 UT). Subsequently, a high plasma-beta region (HB_1) is detected with low He/p values and very low proton temperature. In that respect, FR_1 could be a small-scale FR related to the HPS. Further low plasma-beta, low temperature, and high He/p values give an indication of another FR (FR_2; October 7, 12:15 UT–21:10 UT), with a nonuniform rotational profile as derived from the polar angle θ_B, that is followed by another high plasma-beta region (HB_2). In comparison to HB_1, HB_2 reveals high He/p values and higher temperature; hence, the origin of HB_2 might be different and not related to the HPS. After HB_2 a more pronounced FR (FR_3; October 7, 23:00 UT–October 8, 11:30 UT) is identified, overall revealing typical FR signatures of high He/p, low plasma beta, enhanced magnetic field, linearly decreasing speed profile, and low temperature. With a duration of ≈12.5 hr, FR_3 is at the lower limit of the average duration reported for magnetic ejecta (20.6 ± 9.1 hr; E. K. J. Kilpua et al. 2013). The assignment between the CMEs given in Table 1 and in situ measurements remains speculative. Assuming that FR_1 and HB_1 belong to the HPS, a plausible scenario would be that FR_2 and FR_3 are the compound structures of CME2+3+4, separated by a compression region, HB_2. CME2 and CME3 interacted at approximately 45 R_s, likely forming the complex structure of FR_2. This structure was subsequently interacting with the significantly faster CME4 (FR_3) at about 105 R_s. CME5 and CME6 may not be detected, as predicted. When comparing DBM results and start time of FR_2, we may infer that due to the interaction between HCS and the magnetic structures of CME2+3+4 (2^b+3^b+4^b; see Figure 4), the CMEs were strongly delayed in their arrival by almost 24 hr. In that scenario the shock from CME4 (and maybe also CME5) is propagating ahead of the entire complex of observed HPS-CME structures. The speed profile shows an overall decline from 530 to 410 km s^{-1}, characterized by a plateau over the high plasma-beta region (HB_1) and a monotonic decrease across FR_2 and FR_3. As indicated by the electron PAD, the magnetic sector reversal begins with the shock arrival on October 6 at 07:39 UT and evolves over 48 hr. A stable, outward-directed magnetic field polarity is established during FR_3 and persists thereafter.

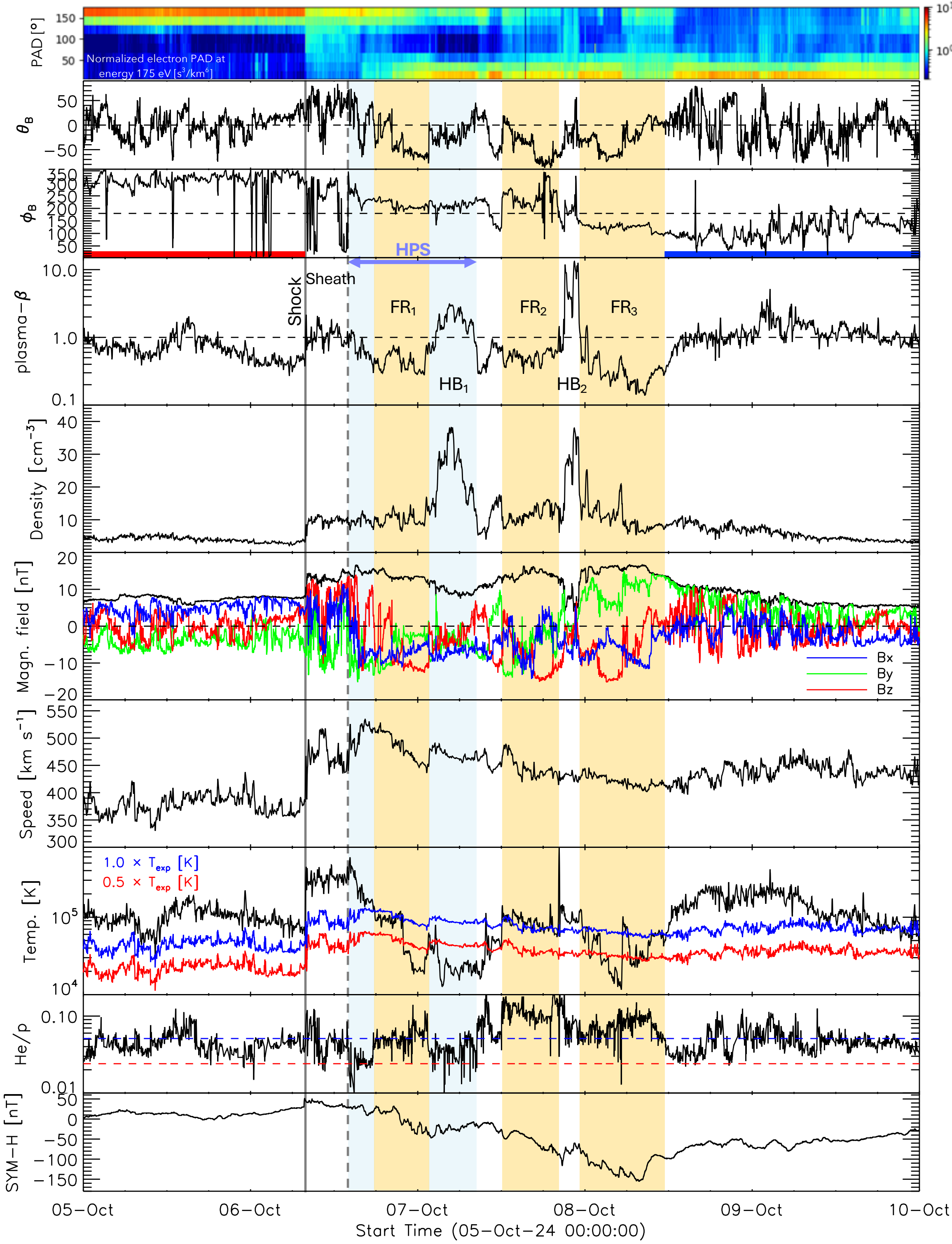

Figure 5. In situ measurements from OMNI in GSE coordinates, covering from top to bottom: electron PADs in the 175 eV energy range (Wind), polar and azimuthal magnetic field direction (θ_B and ϕ_B), plasma beta, proton density, total magnetic field and vector components, proton bulk speed and temperature, He/p density ratio values, and the SYM-H index. The polarity change in the interplanetary magnetic field according to B_x component, electron PAD and ϕ_B is marked in the ϕ_B panel with a red-to-blue bar (inward-to-outward magnetic sector). The temperature panel shows the expected temperature (T_{exp}) in blue and abnormally low temperature ($0.5 \times T_{\mathrm{exp}}$) in red, as taken from solar wind statistics (I. G. Richardson & H. V. Cane 1995). The He/p panel shows thresholds for magnetic ejecta (0.051) and sector-reversal region plasma (0.024) according to statistics by F. Xu & J. E. Borovsky (2015). FR denotes flux rope; HPS denotes heliospheric plasma sheet; HB denotes high plasma-beta region.

To evaluate the geomagnetic response, we examine the SYM-H index (J. A. Wanliss & K. M. Showalter 2006), as shown in the bottom panel of Figure 5. From that we see a standard storm signature, with a sudden storm commencement at the shock arrival, followed by a continuous decline beginning at the arrival of FR_1. The SYM-H index reached its minimum of −148 nT on 2024 October 8, at 8UT, coinciding with the low-temperature region and the maximum southward magnetic field component within FR_3. This can be interpreted as a cumulative effect resulting from the interaction of multiple FRs and the extended duration of the disturbance.

3. Discussion

Between 2024 October 1 and 4, six CMEs as potential Earth-directed events were reported in the CCMC/M2M catalog (see summary in Table 1). Among them is a CME that is related to the X9.0 solar flare that occurred on 2024 October 3, which is confirmed as the strongest solar flare of solar cycle 25 (for details on the solar flare we refer to T. Ding et al. 2025). Along with the intense X7.1 flare-related CME on 2024 October 1, these events originated from the highly active region AR3842 when it was close to the central meridian.

We propagated the six events to 1 au using the DBM, modeling the shock and FR components separately. Estimated arrival times were found to cover the period 2024 October 4–7. Interestingly, CME1, associated with the X7.1 flare, was predicted as an isolated event but likely did not reach Earth, as no indicative in situ signatures were detected within ±24 hr of the predicted arrival time 2024 October 4–5. CMEs 2, 3, and 4 (the latter associated with the X9.0 flare) most likely interacted in interplanetary space and propagated toward Earth as a single entity. CMEs 5 and 6 were predicted to be glancing blows and thus likely did not produce significant in situ signatures. The predicted arrival of CME2+3+4 was temporally associated with the measurement of a crossing of the HCS. This suggests that the HCS may have isolated Earth from the previously launched CME1, making it an opposite-side event, which is characterized by a lack of both in situ signals and geomagnetic effects (see also H. M. Henning et al. 1985; X. Zhao et al. 2007; M. Dumbović et al. 2021). While the preceding structures to CME2+3+4 drive modest activity, the strongest southward fields occur within FR_2 and FR_3, significantly intensifying the storm finally reaching a SYM-H index of −148 nT on 2024 October 8.

The HCS crossing started simultaneously with the arrival of a shock component on 2024 October 6 at 07:39 UT, as deduced from the appearance of the associated geomagnetic sudden storm commencement. This shock is followed by a period of low He/p density ratio, a small-scale FR, FR_1 (October 6, 17:50 UT to October 7, 01:40 UT), and a high plasma-beta region. Subsequently, two additional FRs were identified, FR_2 (October 7, 12:15–21:10 UT) and FR_3 (October 7, 23:00 UT to October 8, 11:30 UT), separated by another high plasma-beta region. These results are generally consistent with existing catalogs. The manually maintained list by I. G. Richardson & H. V. Cane (2010), based on OMNI data, reports the same shock arrival time for the sudden storm commencement on October 6 at 07:39 UT, followed by two consecutive CMEs: the first magnetic ejecta spanning October 6, 14:00 UT to October 7, 20:00 UT, and a second one from October 8, 00:00–11:00 UT. The Helio4Cast catalog (C. Möstl et al. 2020), which employs automated detection of FR signatures (enhanced magnetic field strength and rotation), reports a shock arrival in the Wind data on October 6 at 07:08 UT, followed by three magnetic ejecta: (1) October 6, 15:02 UT to October 7, 00:56 UT; (2) October 7, 11:36–20:20 UT; and (3) October 7, 22:10 UT to October 8, 08:44 UT.

However, our study suggests that FR_1 is an HPS-related structure surrounding the HCS (e.g., B. Lavraud et al. 2020). Besides the in situ measurements, this is supported by the close association between the source region of the CMEs and the HCS, as indicated by the PFSS extrapolation. We may speculate that FR_2, showing a nonuniform rotation in the polar magnetic field angle, might be related to the interacting CMEs 2 and 3. Presumably, because FR_2 is interacting farther out with the faster CME4, i.e., FR_3, the FRs are separated by a strong compression region in between (HB_2). The CME–HCS/HPS complex as such becomes a long-duration magnetic field sector transition event covering more than 48 hr between 2024 October 6 and 8. Previous studies have discussed cases where the HCS does not drape around a CME but rather the CME locally replaces the HCS, resulting in a long-lasting sector reversal (see R. J. Forsyth et al. 1997; N. U. Crooker & T. S. Horbury 2006). Figure 6 illustrates the scenario of the successive CMEs erupting under the HCS structure (right), and replacing the HCS by a closed FR structure (left).

Signatures of the HCS detected within CME structures have been investigated primarily in the CME sheath region, where occasional reconnection signatures point to ongoing interaction processes (M. Ala-Lahti et al. 2025). Due to the draping of the upstream interplanetary magnetic field over the leading edge of the magnetic ejecta, strong compression occurs (see also G. H. Jones et al. 2002), which may result in the ingestion of the warped HCS into the CME sheath (E. K. J. Kilpua et al. 2022). Interaction between the HCS and CME magnetic ejecta has also been observed by multiple spacecraft at different heliocentric distances, revealing changes in the magnetic-field structure induced by the HCS encounter (R. M. Winslow et al. 2016). Recent work by O. M. Romeo et al. (2023) and Y. D. Liu et al. (2024) demonstrates that interactions between CMEs and the HCS result in global restructuring and increased warping of the current sheet.

In this context, we want to emphasize our holistic approach for this study. By examining the source region of the CME, AR3842, our analysis reveals that this region forms part of a nested AR, or active longitude, which has persisted for at least 6 months. This nest appears to be separated in longitude by roughly 180° from a second active longitude responsible for the highly geoeffective 2024 May events (see I. Kontogiannis et al. 2025). Also during solar cycle 23, two active longitudes hosting superactive regions in both hemispheres were reported, separated by about 160°–200° (e.g., A. Q. Chen et al. 2011). The same authors found that these "superactive" regions generate more than 40% of all X-class flares in a solar cycle and that all such regions have the potential to produce fast CMEs capable of driving strong geomagnetic storms. While active longitudes tend to produce high-energy flares and are often associated with strong, magnetically driven CMEs (flare–CME feedback; J. Zhang & K. P. Dere 2006; M. Temmer et al. 2008), they can also significantly shape the global coronal magnetic field (see A. J. Finley 2024). Indeed, from magnetic field extrapolations we find that AR3842 hosts the global neutral line, i.e., the HCS (see Figure 3). Consequently, CME–HCS interaction—or at least, their joint dynamic evolution into complex interplanetary magnetic structures—becomes essentially unavoidable during the maximum activity phase.

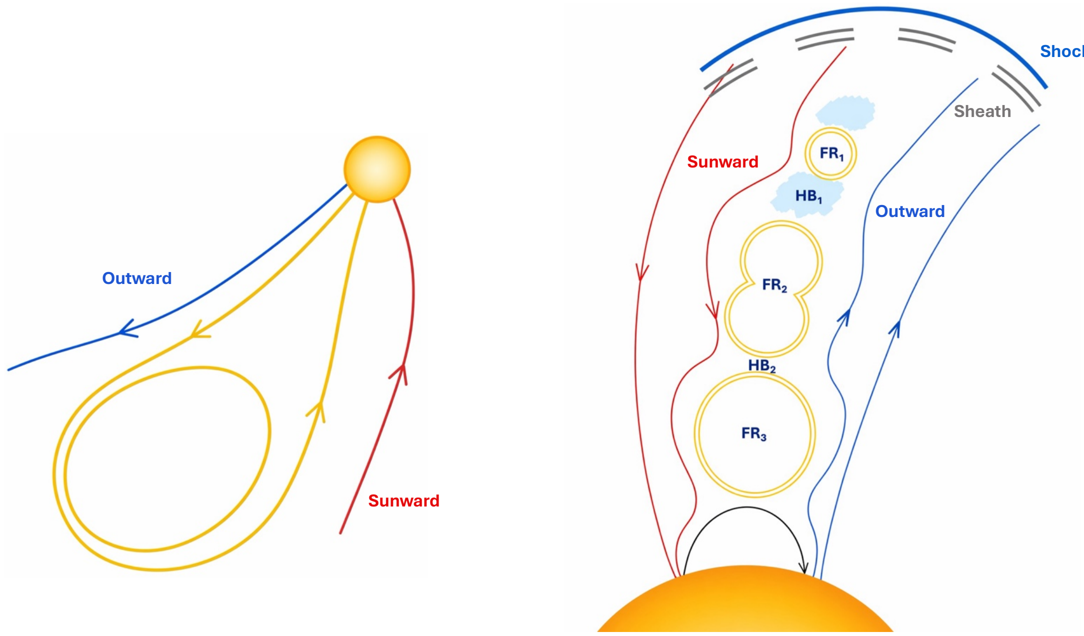

Figure 6. Left: replacement or widening of the HCS by an expanding closed magnetic structure within the HCS (adapted from N. U. Crooker & T. S. Horbury 2006). Right: illustration of the sequence of shock, sheath, flux ropes (FR_1, FR_2, and FR_3), and high plasma-beta structures (HB_1 and HB_2) in between a changing magnetic sector, with blue-shaded areas marking HPS-related structures (see Figure 5).

4. Conclusion

The solar activity period of 2024 October 1–4 caused enhanced geomagnetic activity over 2024 October 5–10 and was driven by a complex “CME-HCS/HPS compound structure” related to the 2024 October 3 event. This complex covers a sequence of FRs and high plasma-beta structures, which eventually replaced or widened the HCS, creating a rare, long-duration magnetic sector transition event lasting over 48 hr. Notably, the CME that launched on 2024 October 1 did not reach Earth as it propagated on the opposite side of the HCS. The study offers a novel holistic perspective by linking such complex events to long-lived nested ARs that persist for months and produce recurrent, highly geoeffective solar events. The study underscores the need to further investigate the dynamic evolution of HCS and HPS-related structures from their active source regions into the heliosphere.

As solar active longitudes and their behavior are found to be similar to stellar activity phenomena (S. V. Berdyugina & I. Tuominen 1998), these results may have broader implications for better understanding the flare–CME relation on magnetically active stars (e.g., F. Koller et al. 2021).

Acknowledgments

We thank the anonymous referee for the valuable comments, which helped improve the study. M.T. and M.D. acknowledge support from the Austrian-Croatian Bilateral Scientific Project “Analysis of solar eruptive phenomena from cradle to grave.” S.G.H. acknowledges funding from the Austrian Science Fund (FWF) Erwin-Schrödinger fellowship [10.55776/J4560] and funding from the Research Council of Finland (Academy Fellowship) [370747; RIB-Wind]. N.D. is grateful for support by the Research Council of Finland (SHOCKSEE, grant No. 346902, and AIPAD, grant No. 368509). E.A. acknowledges support from the Research Council of Finland (Research Fellow grant No. 355659). M.D. acknowledges support from the European Union—NextGenerationEU within the framework of the National Recovery and Resilience Plan (NPOO), project “Eruptive processes on the Sun.” We acknowledge funding from the European Union’s Horizon Europe research and innovation program under grant agreement No. 101134999 (SOLER). The paper reflects only the authors’ view and the European Commission is not responsible for any use that may be made of the information it contains. The authors acknowledge financial support by the University of Graz.

Author Contributions

M.T. initiated the study, performed the main part of the analysis and wrote the manuscript. S.H. provided the analysis for the magnetic-field extrapolation. N.D. and E.A. provided expertise and tools to prepare and interpret 3DP data. All authors discussed and proofread the manuscript.

ORCID iDs

Manuela Temmer https://orcid.org/0000-0003-4867-7558
Stephan G. Heinemann https://orcid.org/0000-0002-2655-2108
Nina Dresing https://orcid.org/0000-0003-3903-4649
Mateja Dumbovic https://orcid.org/0000-0002-8680-8267
Eleanna Asvestari https://orcid.org/0000-0002-6998-7224

References

Ala-Lahti, M., Pulkkinen, T. I., Suni, J., et al. 2025, ApJL, 994, L30
Arge, C. N., Henney, C. J., Koller, J., et al. 2010, AIPC, 1216, 343
Auchère, F., Cook, J. W., Newmark, J. S., et al. 2005, ApJ, 625, 1036
Berdyugina, S. V., & Tuominen, I. 1998, A&A, 336, L25
Berdyugina, S. V., & Usoskin, I. G. 2003, A&A, 405, 1121
Blanco, J. J., Hidalgo, M. A., Rodriguez-Pacheco, J., & Medina, J. 2011, JASTP, 73, 1339
Brueckner, G. E., Howard, R. A., Koomen, M. J., et al. 1995, SoPh, 162, 357
Čalogović, J., Dumbović, M., Sudar, D., et al. 2021, SoPh, 296, 114
Chen, A. Q., Wang, J. X., Li, J. W., Feynman, J., & Zhang, J. 2011, A&A, 534, A47
Cremades, H., Bothmer, V., & Tripathi, D. 2006, AdSpR, 38, 461

Crooker, N. U., & Horbury, T. S. 2006, SSRv, 123, 93
de Toma, G., White, O. R., & Harvey, K. L. 2000, ApJ, 529, 1101
Ding, T., Zhang, J., & Hou, Y. 2025, ApJL, 985, L16
Domingo, V., Fleck, B., & Poland, A. I. 1995, SoPh, 162, 1
Dumbović, M., Čalogović, J., Martinić, K., et al. 2021, FrASS, 8, 58
Dumbović, M., Veronig, A. M., Podladchikova, T., et al. 2021, A&A, 652, A159
Finley, A. J. 2024, A&A, 692, A29
Finley, A. J., Brun, A. S., Strugarek, A., & Perri, B. 2025, A&A, 697, A217
Forsyth, R. J., Balogh, A., Smith, E. J., & Gosling, J. T. 1997, GeoRL, 24, 3101
Gaizauskas, V., Harvey, K. L., Harvey, J. W., & Zwaan, C. 1983, ApJ, 265, 1056
Gopalswamy, N., Mäkelä, P., Xie, H., Akiyama, S., & Yashiro, S. 2009, JGRA, 114, A00A22
Guo, J., Dumbović, M., Wimmer-Schweingruber, R., et al. 2018, SpWea, 16, 8
Harvey, J. W., Hill, F., Hubbard, R. P., et al. 1996, Sci, 272, 1284
Hayakawa, H., Ebihara, Y., Mishev, A., et al. 2025, ApJ, 979, 49
Heinemann, S. G., Pomoell, J., Caplan, R. M., et al. 2025, ApJ, 986, 166
Heinemann, S. G., Temmer, M., Farrugia, C. J., et al. 2019, SoPh, 294, 121
Henning, H. M., Scherrer, P. H., & Hoeksema, J. T. 1985, JGR, 90, 11055
Howard, T. A., & Tappin, S. J. 2005, A&A, 440, 373
Jones, G. H., Rees, A., Balogh, A., & Forsyth, R. J. 2002, GeoRL, 29, 1520
Kilpua, E. K. J., Good, S. W., Ala-Lahti, M., et al. 2022, A&A, 663, A108
Kilpua, E. K. J., Isavnin, A., Vourlidas, A., Koskinen, H. E. J., & Rodriguez, L. 2013, AnGeo, 31, 1251
King, J. H., & Papitashvili, N. E. 2005, JGRA, 110, A02104
Koller, F., Leitzinger, M., Temmer, M., et al. 2021, A&A, 646, 22
Kontogiannis, I., Zhu, Y., Barczynski, K., et al. 2025, A&A, 704, A105
Lavraud, B., Fargette, N., Réville, V., et al. 2020, ApJL, 894, L19
Lemen, J. R., Title, A. M., Akin, D. J., et al. 2012, SoPh, 275, 17
Lin, R. P., Anderson, K. A., Ashford, S., et al. 1995, SSRv, 71, 125
Liu, Y., Luhmann, J., Möstl, C., et al. 2012, ApJL, 746, L15
Liu, Y. D., Zhu, B., Ran, H., et al. 2024, ApJ, 963, 85
Loumou, K., Hannah, I. G., & Hudson, H. S. 2018, A&A, 618, 12
Lugaz, N., Farrugia, C. J., Smith, C. W., & Paulson, K. 2015, JGRA, 120, 2409
Millward, G., Biesecker, D., Pizzo, V., & de Koning, C. A. 2013, SpWea, 11, 57
Möstl, C., Weiss, A. J., Bailey, R. L., et al. 2020, ApJ, 903, 92
Ogilvie, K. W., & Desch, M. D. 1997, AdSpR, 20, 559
Owens, M. J., & Forsyth, R. J. 2013, LRSP, 10, 52
Pesnell, W. D., Thompson, B. J., & Chamberlin, P. C. 2012, SoPh, 275, 3
Richardson, I. G., & Cane, H. V. 1995, JGRA, 100, 23397
Richardson, I. G., & Cane, H. V. 2010, SoPh, 264, 189
Romeo, O. M., Braga, C. R., Badman, S. T., et al. 2023, ApJ, 954, 168
Sammis, I., Tang, F., & Zirin, H. 2000, ApJ, 540, 583
Schou, J., Scherrer, P. H., Bush, R. I., et al. 2012, SoPh, 275, 229
Svalgaard, L., & Wilcox, J. M. 1976, SoPh, 49, 177
Temmer, M., Dumbović, M., Martinić, K., et al. 2025, A&A, 695, A58
Temmer, M., Veronig, A. M., Vršnak, B., et al. 2008, ApJL, 673, L95
Usoskin, I. G., Berdyugina, S. V., & Poutanen, J. 2005, A&A, 441, 347
van Driel-Gesztelyi, L., & Green, L. M. 2015, LRSP, 12, 1
Vršnak, B., Temmer, M., Žic, T., et al. 2014, ApJS, 213, 21
Vršnak, B., Žic, T., Vrbanec, D., et al. 2013, SoPh, 285, 295
Wanliss, J. A., & Showalter, K. M. 2006, JGRA, 111, A02202
Wilson, L. B., III, Brosius, A. L., Gopalswamy, N., et al. 2021, RvGeo, 59, e2020RG000714
Winslow, R. M., Lugaz, N., Schwadron, N. A., et al. 2016, JGRA, 121, 6092
Xu, F., & Borovsky, J. E. 2015, JGRA, 120, 70
Yurchyshyn, V. B., Wang, H., Goode, P. R., & Deng, Y. 2001, ApJ, 563, 381
Zhang, J., & Dere, K. P. 2006, ApJ, 649, 1100
Zhang, J., Richardson, I. G., Webb, D. F., et al. 2007, JGRA, 112, A10102
Zhao, X., Feng, X., & Wu, C.-C. 2007, JGRA, 112, A06107
Zurbuchen, T. H., & Richardson, I. G. 2006, SSRv, 123, 31